UDC 539.4

Effect of the Interfacial Transition Zone on Basic Mechanical Properties of a Solid Composite Propellant

L. L. Shen,[a] Z. B. Shen,[a,1] H. R. Cui,[a] H. Y. Li,[a] and S. J. Zhi[b]

[a] College of Aeronautics and Astronautics, National University of Defense Technology, Changsha, Hunan, China

[b] China Airborne Missile Academy, Luoyang, Henan, China

[1] zb_shen@yeah.net

The evaluation of basic mechanical properties are shown to be of importance for the solid composite propellant development and application. The numerical analysis approach termed the three-phase Voronoi cell finite element method, was proposed to evaluate of the interfacial transition zone effect. Numerical results showed that the performance of the effective modulus could be essentially enhanced by increasing the zone thickness. The module of the composite with the inhomogeneous zone was higher than that of the composite with the homogeneous one. The effect of different zones on volume fractions and matrix moduli was also calculated. The Voronoi method can also be helpful for analyzing the characteristic properties of other three-phase composites.

Keywords: solid composite propellant, Voronoi cell finite element method, interfacial transition zone.

Introduction. Composite solid propellant (CSP) is a complex particulate reinforced material [1]. Its effective mechanical constants are critical for estimating the structural integrity and the service life of propellant grains [2]. Currently, the inclusion particle and matrix binders are ammonium perchlorate (AP) and hydroxyl-terminated polybutadiene (HTPB) in industrial field respectively. Besides, bonding agents including nitrogen heterocyclic ring compound are added to CSP to form an organic layer, i.e., interfacial transition zone (ITZ), surrounding with AP particles to avoid dewetting [3]. The ITZ is regarded as the third phase in micromechanics analysis and has a significant influence on the macroscopic behavior of material generally. Hence, it is crucial to model a microstructure of CSP considering the third phase to estimate its mechanical properties in an accurate way.

The working mechanism and influence law of ITZ have drawn interests of scholars engaged into studying composite materials. Theoretical derivation methods [4, 5], microstructure graphic processing methods [6, 7] and regular material tests [8–10] are applied widely to reveal the relationship between mechanical properties of polymer materials and microscopic characteristics of ITZ. It is noteworthy that the numerical simulation method [11–13] is becoming one of the main approaches to realize multi-scale modeling and characterizing of materials with ITZ in recent years own to its advantages such as low cost, short period and intuitive expression. The displacement-based finite element method (FEM) is a commonly used numerical method in engineering field now. However, this method requires a lot of complex grid elements and huge computational costs to characterize a thin interface between the particle and matrix. A new numerical method is urgently needed to study ITZ problems.

Voronoi cell finite element method (VCFEM) is a promising numerical analysis tool. It characters the microstructure of CSP with Voronoi tessellations [14] and achieves the stress filed and nodal displacement of each element by a hybrid stress element method [15]. The number of elements required for VCFEM is equal to the number of inclusions and

could be far less than that needed for FEM. Therefore, this method can improve the computational efficiency and address some problems that other methods cannot solve correctly. An irreplaceable contribution of developing VCFEM to analyze the heterogeneous material has been made by Ghosh and his co-works over the last two decades [16–20]. However, they did not apply the method to study three-phase materials in the published literature.

Some new efforts are made to understand the effect of ITZ in this paper. The finite element formulation of three-phase VCFEM is extended based on the past work [21] in the second section. The feasibility and validity of this method are demonstrated by comparison with classical FEM. Besides, a microstructure model is reconstructed with the micro-CT scanning of real propellant. Then effect analyses of ITZ thickness and material properties on effective mechanical constants of CSP are carried out.

1. **Mathematical Model**. Each Voronoi cell is a convex polygon and corresponds to a seed point. Voronoi diagram is suitable to characterize the microstructural morphology of particle composites, because the microscopic model can be divided into Voronoi cells based on the position of the particles. The total amount of Voronoi cells is the same as that of particles. Except for the matrix phase, there are an inclusion phase and an ITZ phase in each Voronoi cell, as shown in Fig. 1. Obtain the stiffness matrix of each element by a hybrid stress method and assemble it into a global stiffness matrix. Finally, the nodal displacement and other mechanical properties can be achieved with the global stiffness matrix.
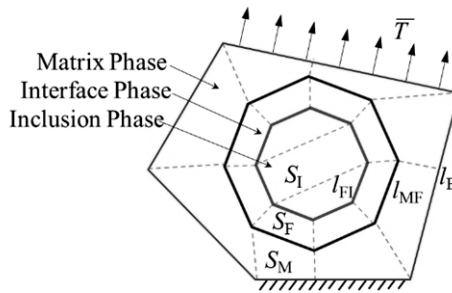
Fig. 1. A basic Voronoi cell with three phases.

1.1. *Element Stiffness Matrix*. The element formulation of each Voronoi cell is derived based on the principle of minimum complementary energy [16]. For linear elastic problems, the complementary energy functional for a two-dimensional element has the form as follows:

$$\Pi_e = -\int_{\Omega_e} \frac{1}{2} \sigma^T S \sigma d\Omega + \int_{\Gamma_e} (n\sigma)^T u d\Gamma - \int_{\Gamma_T} \overline{T} u d\Gamma, \tag{1}$$

where σ is the equilibrium stress field in the element domain Ω_e, u is the compatible displacement field on the element boundary $\partial \Omega_e$ with an outward normal n, $\overline{T}$ is the prescribed traction on Γ_T the element boundary that coincides with global traction boundary, and S is the elastic compliance matrix. It is a matrix containing the Young modulus E and Poisson's ratio v:

$$S = \frac{1}{E} \begin{bmatrix} 1 & -v & 0 \\ -v & 1 & 0 \\ 0 & 0 & 2(1+v) \end{bmatrix}. \tag{2}$$

The traction compatibility condition on the matrix–ITZ and ITZ–inclusion interface can be expressed as

$$\sigma^M - \sigma^F = 0 \quad \text{on} \quad \partial\Omega_{MF},$$
$$\sigma^F - \sigma^1 = 0 \quad \text{on} \quad \partial\Omega_{FI}. \tag{3}$$

Lagrange multipliers are used to ensure traction continuity constraint along the matrix–ITZ and ITZ–inclusion interface, Eq. (1) is enhanced as

$$\Pi_e^*(\sigma^{M/F/I}, \boldsymbol{u}^{E/MF/FI}) = \int_{\Omega_M} \frac{1}{2}(\sigma^M)^T \boldsymbol{S}^M \sigma^M \, d\Omega + \int_{\Omega_F} \frac{1}{2}(\sigma^F)^T \boldsymbol{S}^F \sigma^F \, d\Omega +$$

$$+ \int_{\Omega_I} \frac{1}{2}(\sigma^I)^T \boldsymbol{S}^I \sigma^I \, d\Omega - \int_{\partial\Omega_E} (\boldsymbol{n}^E \sigma^M)^T \boldsymbol{u}^E \, d\Gamma + \int_{\Gamma_T} \overline{\boldsymbol{T}}^T \boldsymbol{u}^E \, d\Gamma +$$

$$+ \int_{\partial\Omega_{MF}} \Gamma(\boldsymbol{n}^{MF}(\sigma^M - \sigma^F))^T \boldsymbol{u}^{MF} \, d\Gamma + \int_{\partial\Omega_{FI}} (\boldsymbol{n}^{FI}(\sigma^F - \sigma^I))^T \boldsymbol{u}^{FI} \, d\Gamma, \tag{4}$$

where these variables with the superscripts *M*, *F*, and *I* correspond to the interior of the matrix, ITZ, and inclusion phases, respectively, while subscripts or superscripts *E*, *MI*, and *FI* refer to variables on the element boundary, internal matrix–ITZ interface, and ITZ–inclusion interface, respectively.

In the application of variation principles, the equilibrating stress field is expressed as a polynomial in the interior of the element as

$$\sigma^{M/F/I} = \boldsymbol{P}^{M/F/I} \beta^{M/F/I} \quad \text{in} \quad \Omega_{M/F/I}, \tag{5}$$

where for two-dimensional problems σ is a column vector of three stress components, β is a column of *m* undetermined stress coefficients β_1, β_2, ..., β_m. $\boldsymbol{P}$ is a $3 \times m$ interpolation matrix based on the partial derivative of the complete polynomial stress function as reported in [15]. The boundary displacements can be interpolated from the generalized displacement at the nodes, in the form

$$\boldsymbol{u}^{E/MF/FI} = \boldsymbol{L}^{E/MF/FI} \boldsymbol{q}^{E/MF/FI} \quad \text{on} \quad \partial\Omega_{E/MF/FI}, \tag{6}$$

where $\boldsymbol{q}$ is the nodal displacement and the matrix $\boldsymbol{L}$ is composed of functions of boundary coordinates as reported in [15].

Similarly, the load vector is denoted as

$$\boldsymbol{Q} = \int_{\Gamma_T} \overline{\boldsymbol{T}}^T \boldsymbol{L} d\Gamma. \tag{7}$$

Substituting Eqs. (5)–(7) into Eq. (4), the Π_e can be simplified as

$$\Pi_e(\beta, \boldsymbol{q}) = \frac{1}{2}\beta^T \boldsymbol{H}\beta - \beta^T \boldsymbol{G}\boldsymbol{q} + \boldsymbol{Q}\boldsymbol{q}, \tag{8}$$

where those vectors are defined as

$$\beta = (\beta^M \quad \beta^F \quad \beta^I)^T, \qquad q = (q^E \quad q^{MF} \quad q^{FI})^T, \qquad Q = (Q^E \quad Q^{MF} \quad Q^{FI})^T.$$

The matrices H and G are defined as

$$H = \begin{bmatrix} H^M & 0 & 0 \\ 0 & H^F & 0 \\ 0 & 0 & H^I \end{bmatrix}, \qquad G = \begin{bmatrix} G^E & -G^{MF} & 0 \\ 0 & G^{MF} & -G^{FI} \\ 0 & 0 & G^{FI} \end{bmatrix},$$

where

$$H^{M/F/I} = \int_{\Omega_{M/F/I}} [P^{M/F/I}]^T S^{M/F/I} P^{M/F/I} \, d\Omega, \tag{9}$$

$$G^{E/MF/FI} = \int_{\partial\Omega_{E/MF/FI}} [P^{E/MF/FI}]^T [n^{E/MF/FI}]^T L^{E/MF/FI} \, d\Gamma. \tag{10}$$

Considering the stable condition of the total complementary energy, we can get $\partial\Pi_e^* / \partial\beta = 0.$ Consequently, the vectors β are expressed as

$$\beta = H^{-1}Gq. \tag{11}$$

Substituting Eq. (11) into Eq. (8) and setting the first order partial differential $\partial\Pi_e^* / \partial q = 0$ gives

$$K_e q = Q, \tag{12}$$

where $K_e = G^T H^{-1} G.$

1.2. **Solution Formulation**. The additional displacement constraints are imposed to avoid rigid body displacement by introducing a Lagrange multiplier λ

$$\begin{bmatrix} K_e & \Phi^T \\ \Phi & 0 \end{bmatrix} \begin{Bmatrix} q \\ \lambda \end{Bmatrix} = \begin{Bmatrix} Q \\ 0 \end{Bmatrix}, \tag{13}$$

where Φ can be expressed as

$$\Phi = \begin{bmatrix} 0 & \{(\varphi^{MF})^T \varphi^{MF}\}^{-1}(\varphi^{MF})^T & -\{(\varphi^{FI})^T \varphi^{FI}\}^{-1}(\varphi^{FI})^T \\ \{(\varphi^E)^T \varphi^E\}^{-1}(\varphi^E)^T & -\{(\varphi^{MF})^T \varphi^{MF}\}^{-1}(\varphi^{MF})^T & 0 \end{bmatrix}, \tag{14}$$

where

$$\varphi^{E/MF/FI} = \begin{bmatrix} 1 & 0 & 1 & 0 & \dots & 1 & 0 \\ 0 & 1 & 0 & 1 & \dots & 0 & 1 \\ -y_1 & x_1 & -y_2 & x_2 & \dots & -y_n & x_n \end{bmatrix}^T,$$

x_i and y_i are the coordinate value of the ith node.

When the nodes of the interface are not connected with those of element boundary, the displacements of inner nodes are not affected by other elements directly. The nodal displacements of the matrix–ITZ interface can be represented by nodal displacements of

element boundary. Therefore, the stiffness matrix of elements can be eliminated to reduce the computing scale as follows:

$$\boldsymbol{K}_e^* = \boldsymbol{K}_{11} - \boldsymbol{K}_{12}^* (\boldsymbol{K}_{22}^*)^{-1} (\boldsymbol{K}_{12}^*)^T , \tag{15}$$

where

$$\boldsymbol{K}_{12}^* = [\boldsymbol{K}_{12} \quad \boldsymbol{0} \quad \boldsymbol{0} \quad (\{(\varphi^E)^T \varphi^E\}^{-1} (\varphi^E)^T)^T], \tag{16}$$

$$\boldsymbol{K}_{22}^* = \begin{bmatrix} \boldsymbol{K}_{22}^{**} & (-\{(\varphi^{MF})^T \varphi^{MF}\}^{-1} (\varphi^{MF})^T)^T \\ -\{(\varphi^{MF})^T \varphi^{MF}\}^{-1} (\varphi^{MF})^T & \boldsymbol{0} \end{bmatrix}. \tag{17}$$

In the same way, the nodal displacements of the matrix–ITZ interface can be represented by those of ITZ–inclusion interface. So the stiffness matrix of the element can be reduced to

$$\boldsymbol{K}_{22}^{**} = \boldsymbol{K}_{22} - \boldsymbol{K}_{23}^* (\boldsymbol{K}_{33}^*)^{-1} (\boldsymbol{K}_{23}^*)^T , \tag{18}$$

where

$$\boldsymbol{K}_{23}^* = [\boldsymbol{K}_{23} \quad (\{(\varphi^{MF})^T \varphi^{MF}\}^{-1} (\varphi^{MF})^T)^T], \tag{19}$$

$$\boldsymbol{K}_{33}^* = \begin{bmatrix} \boldsymbol{K}_{33} & (-\{(\varphi^{FI})^T \varphi^{FI}\}^{-1} (\varphi^{FI})^T)^T \\ -\{(\varphi^{FI})^T \varphi^{FI}\}^{-1} (\varphi^{FI})^T & \boldsymbol{0} \end{bmatrix}. \tag{20}$$

Loads of inner nodes are equal to zero generally. Therefore, corresponding mechanical load vectors can be reduced to the following form:

$$\boldsymbol{Q}_e^* = \boldsymbol{Q}^E. \tag{21}$$

Finally, assembling stiffness matrices and mechanical load vectors of all elements

$$\boldsymbol{K}^* = \sum_{i=1}^{n} (\boldsymbol{K}_e^*)_i , \qquad \boldsymbol{Q}^* = \sum_{i=1}^{n} (\boldsymbol{Q}_e^*)_i . \tag{22}$$

The nodal displacements are solutions of the following equation:

$$\boldsymbol{K}^* \boldsymbol{q}^* = \boldsymbol{Q}^*. \tag{23}$$

The inner nodal displacements of the element can be easily obtained by

$$\begin{aligned} \boldsymbol{q}^{MF} &= (\boldsymbol{K}_{22}^*)^{-1} (\boldsymbol{K}_{12}^*)^T \boldsymbol{q}^E , \\ \boldsymbol{q}^{FI} &= (\boldsymbol{K}_{33}^*)^{-1} (\boldsymbol{K}_{23}^*)^T \boldsymbol{q}^{MF} . \end{aligned} \tag{24}$$

After getting the value of β by Eq. (11), the stress field of every phase can be achieved by Eq. (5).

1.3. *Variations in Material Constants of ITZ*. The Young modulus E in Eq. (2) is replaced by a function of r, that is $E_F = E(r)$, where r is the distance from the center of inclusion. The material constants of inclusion are entirely different from those of the
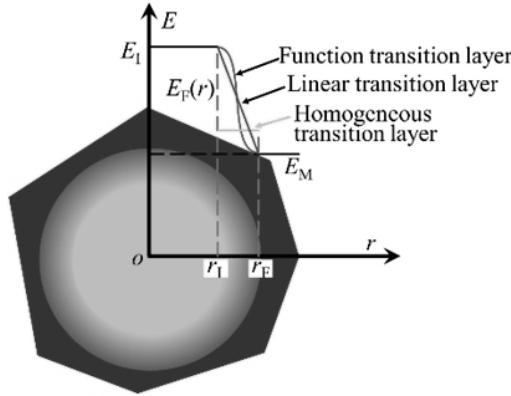
Fig. 2. Sketch of the variation of the Young modulus of ITZ.

matrix. So the ITZ is considered as the transition phase between these two phases. The material constants of ITZ near the interface are closed to those of its neighbor phase. As shown in Fig. 2, to represent the transitivity and inhomogeneity of ITZ, the following two variations in EF are used:

1. Linear variation

$$E_F(r) = E_I - \frac{E_I - E_M}{r_F - r_I}(r - r_I). \tag{25}$$

2. Cosine variation

$$E_F(r) = \frac{E_I + E_M}{2} + \frac{E_I - E_M}{2} \cos \frac{\pi}{r_F - r_I}(r - r_I). \tag{26}$$

The results of these equations are equal to the corresponding phase modulus when the r is r_F or r_I. Some authors employed cubic variation to describe the variation in the material of ITZ [22]:

$$E_F(r) = C_0 + C_1 r + C_2 r^2 + C_3 r^3, \tag{27}$$

where C_0, C_1, C_2, and C_3 are constants which are determined from the conditions on constants E_M, E_I, r_I, and r_F. Since moduli have smooth transitions at the boundaries, first derivatives of $E_F(r)$ are equal to zero at the particle/ITZ and ITZ/matrix boundaries. Coefficients of Eq. (27) can achieved by solving follow four equations: $E_F(r_F) = E_M$, $E_F(r_I) = E_I$, $(E_F(r_F))' = 0$, and $(E_F(r_I))' = 0$. The almost similar variation curve with cubic variation can be obtained by adopting cosine variation directly without solving equations. Therefore, the cosine function is selected to characterize the variation here.

2. **Numerical Implementation**.

2.1. *Numerical Procedures*. FORTRAN programming language is used to realize the core numeric computation. The computational workflow and the interactions between the different numerical procedures are shown in Fig. 3. The pre-processing and post-processing are simulated in MATLAB.

To construct the matrix **H** and matrix **D**, an integration regions subdivision scheme is proposed here to compute the numerical area integration of each phase with Eqs. (9) and (10). As shown in Fig. 1, regular octagons are used to simulate the circular inclusions and ITZs. New nodes are added on element boundaries for the cell to own eight nodes (red nodes). The line segments connecting the cell nodes and corresponding ITZ node divide the
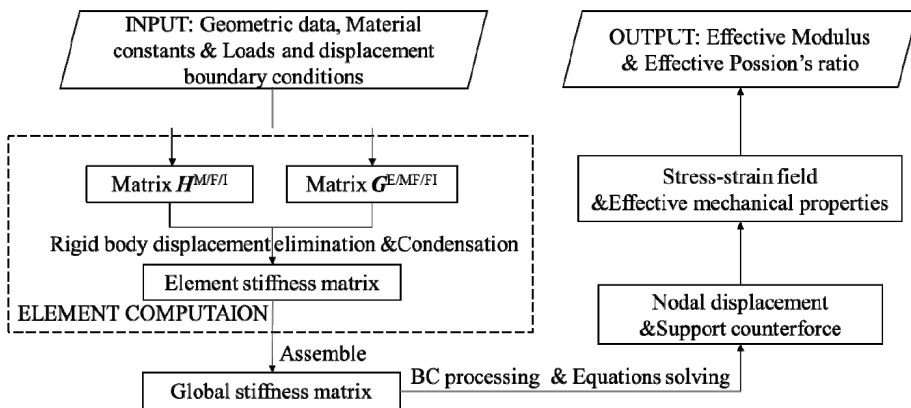
Fig. 3. Computational flowchart of the numerical procedure.

matrix phase into eight quadrilateral integration regions (red lines). Similarly, ITZ phase can also be divided into eight quadrilateral integration regions (blue lines). The octagon inclusion phase is subdivided into three quadrilateral integration region (yellow lines). Convergence of this model is achieved by conducting numerical experiments with 25 β parameters for the stress interpolation in Eq. (5).

2.2. *Validation*. In an attempt to verify the accuracy of 3P-VCFEM, a basic cell is designed in this part. Results obtained by the 3P-VCFEM and the commercial code based FEM are compared. The Young moduli of matrix phase, ITZ phase, and inclusion phase are 1000, 2000, and 3000 MPa, respectively. The Poisson's ratio of three phase is 0.2. The geometry size and loading condition are shown in Fig. 4a. The node number of VCFEM mesh is shown in Fig. 4c. 4480, 1713, and 2304 linear quadrilateral elements are used to mesh matrix phase, ITZ phase and inclusion phase in FEM respectively as displayed in Fig. 4d.

The deformation pattern obtained by VCFEM is plotted in Fig. 4b. It can be concluded that the deformation of the entire model is symmetrical and reasonable. The displacement of the interface between different phases is maintained compatibly. Furthermore, displacements of critical nodes obtained by VCFEM and FEM are listed in Table 1. The greatest normalized error of the two methods is less than 5%. It shows good agreements between the displacement results of VCFEM and FEM, even though the quantity of elements for FEM mesh is far larger than that of the VCFEM mesh.

3. **Examples and Discussion**. Bonding agent that is a kind of surface-active molecules will produce physical adsorption and chemical reaction with the oxidizer to assembling on the surface of particle oxidizer. On the other hand, the bonding agent can access the matrix network structure by forming chemical bonds with matrix binder. Finally, a high modulus layer will be shaped around every solid particle to avoid the problem of interfacial dewetting and to improve the mechanical properties of propellant. This layer is called the interfacial transition zone (ITZ) because it is between the inclusion and matrix phases. The thickness and mechanical properties of ITZ are mainly subject to the dosage and category of bonding agents. If we establish a relationship between ITZ and effective mechanical properties, we can design propellants by controlling the dosage of bonding agents.

CSP can be assumed consist of HTPB binder and AP particles of approximately the same size as shown in Fig. 5a. Based on this hypothesis, an RVE (representative volume element) with 39 Voronoi cells is constructed here based on optimal equal circle packing schemes as shown in Fig. 5b. The inclusion circles are matched by regular octagons. The radius of the circumscribed circle of octagons is 210 μm. The ITZ node is on the extension

T a b l e 1

Nodal Displacements of Different Phases of Two Numerical Methods

Node ID	VCFEM			FEM			Normalized error (%)		
	Matrix	ITZ	Inclusion	Matrix	ITZ	Inclusion	Matrix	ITZ	Inclusion
1	0.0069	0.0074	0.0073	0.0071	0.0070	0.0069	1.55	2.24	2.62
2	0.0161	0.0098	0.0088	0.0163	0.0098	0.0085	1.80	0.18	1.96
3	0.0120	0.0105	0.0095	0.0122	0.0100	0.0089	1.50	3.19	3.91
4	0.0161	0.0098	0.0088	0.0163	0.0098	0.0085	1.80	0.17	2.01
5	0.0069	0.0074	0.0073	0.0071	0.0070	0.0069	1.55	2.24	2.62
6	0.0000	0.0048	0.0057	0.0000	0.0041	0.0051	0	4.08	3.51
7	0.0000	0.0034	0.0047	0.0000	0.0028	0.0042	0	3.60	2.83
8	0.0000	0.0048	0.0057	0.0000	0.0041	0.0051	0	4.08	3.52
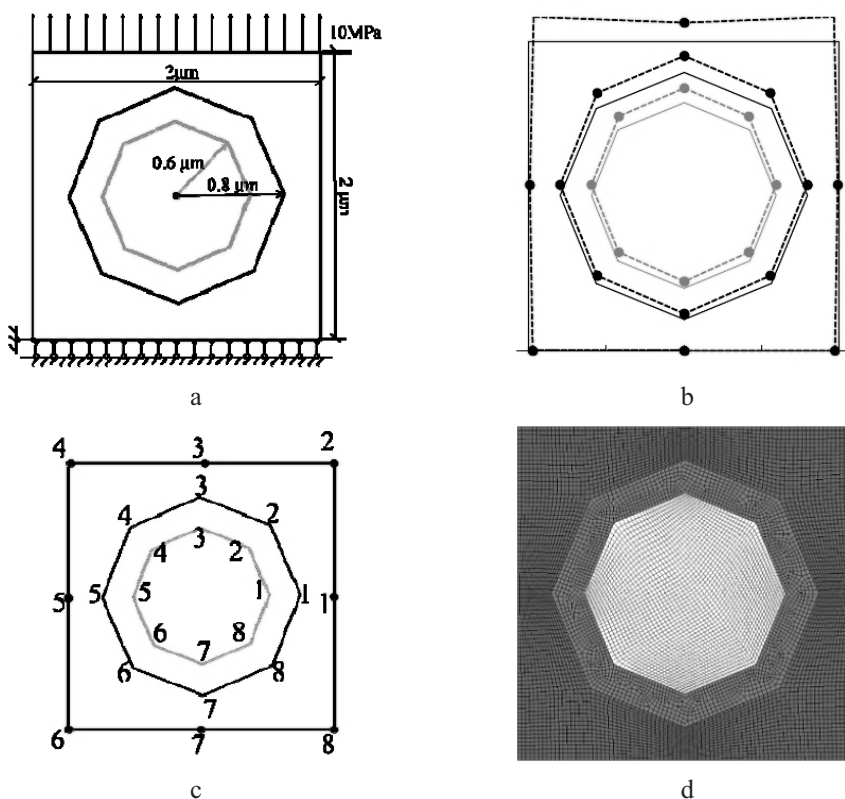
Fig. 4. The base cell with regular octagon ITZ and inclusion: (a) geometry and loading condition; (b) deformation pattern; (c) VCFEM mesh; (d) FEM mesh.

line of corresponding inclusion node and seed point. The inclusion volume fraction is 54%, and the ITZ thickness is 6 μm in the absence of special instructions in below examples.

The matrix binder is considered as a hyperelastic material: $E_M = 7.39$ MPa, $\nu_M = 0.45$. The inclusion particle is an elastic material with high stiffness: $E_I = 68.3$ GPa, $\nu_I = 0.14$. The Poisson's ratio of ITZ is 0.33. Besides, the module of ITZ is set as a

a   b
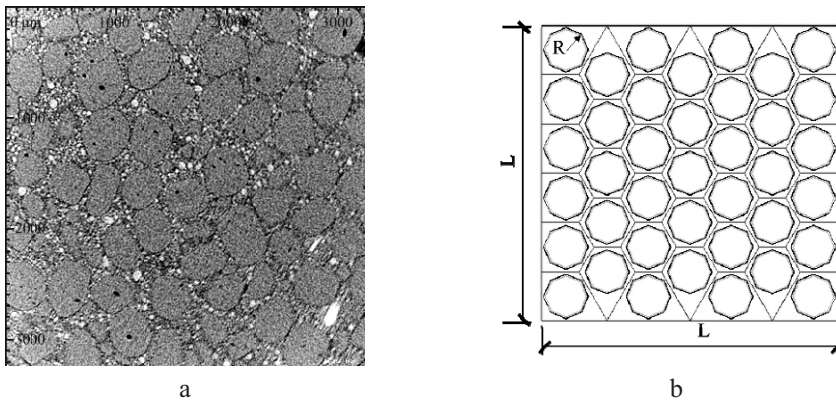
Fig. 5. The microstructure of CSP: micro-CT scanning (a) and RVE model (b).
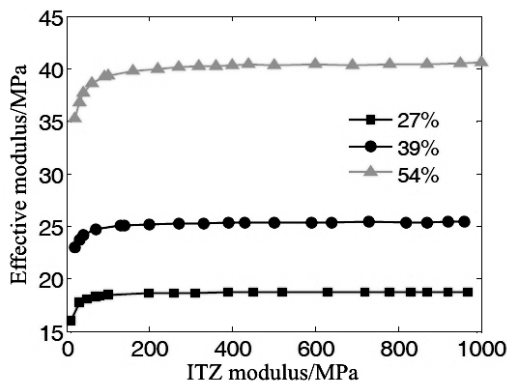
Fig. 6. Effective modulus versus ITZ modulus.

constant and varied in radial direction respectively. The effective moduli of composites with different ITZ moduli are compared to select the appropriate modulus constant of homogeneity ITZ. As shown in Fig. 6, the increase of ITZ modulus has a weak effect on the effective modulus when it exceeds a value. Hence, the modulus of homogeneity ITZ is taken as 1000 MPa in below numerical examples. The effect of thickness and inhomogeneity of ITZ on the effective mechanical properties are studied for the realistic demand by following numerical examples. The experimental results and theoretical models indicate that inclusion volume fraction and matrix modulus are key factors controlling the effective mechanical properties [21, 23]. In Figs. 7–9, the difference value is the absolute value of the result of an effective property of inhomogeneous ITZ composite minus that of homogeneous ITZ composite. The relative different refers to the percentage of the different value divided by the effective property of homogeneous ITZ composite.

3.1. *Effect of ITZ Thickness*. To explore the influence law of ITZ thickness, effective mechanical properties of composites with several thicknesses ranging from $t = 30 \, \mu$m to $t = 0$ (no ITZ case) have been analyzed. In Fig. 7, we can note that the thicker the ITZ, the higher is the effective modulus. It means that the presence of ITZ can further strengthen the inclusion enhancement-effect of CSP. When ITZ is thick, the effective modulus of composites with inhomogeneous ITZ is slightly larger than that of composites of homogeneous ITZ. On the other hand, the apparent differences between no ITZ case and different thickness ITZ cases indicate that the estimated results of CSP will not be precise enough without regard to the influence of ITZ.
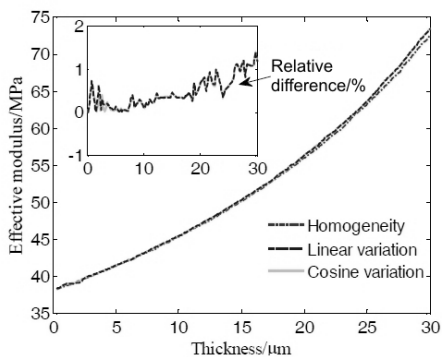
Fig. 7. Effect of ITZ thickness on the effective modulus of CSP.

3.2. *Effect of Inclusion Volume Fraction*. Comparison of effective properties between the inhomogeneous (linear variation and cosine variation) and homogeneous ITZ cases is showed in Fig. 8. With the increase of inclusion volume fraction, the same tendency of three curves is observed. With the growth of volume fraction of inclusion, the effective modulus increases while Poisson's ratio decreases. The effective moduli of homogeneous ITZ composites are smaller than that of inhomogeneous ITZ composites when the volume fraction is high as shown in Fig. 8a. However, there is no apparent difference between Poisson's ratios of composites with three kinds ITZs in Fig. 8b.

a

b
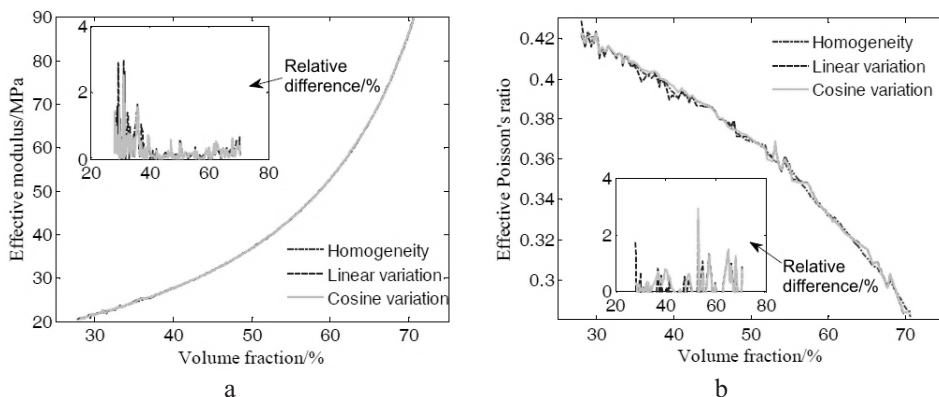
Fig. 8. Effect of volume fraction on the mechanical properties of CSP: (a) effective modulus; (b) effective Poisson's ratio.

3.3. *Effect of Matrix Modulus*. As shown in Figs. 7 and 8, relative differences in the above two cases are less than 4%. It initiates effective properties of different ITZ composites are close. We wonder if this because the matrix material is much softer than inclusion material in CSP. The effective moduli of composites with different matrix modulus are calculated (Fig. 9a). With the increase of matrix modulus, the difference between homogeneous ITZ composites and inhomogeneous ITZ composites is getting larger. However, there is no significant difference between the composites with two different inhomogeneous ITZ. Furthermore, a plot using a base 10 logarithmic scale for matrix modulus and linear scale for different relative displays in Fig. 9b. We can note the relative error is less than 4% when matrix modulus is below 1000 MPa. The matrix modulus of solid propellants is always less than 100 MPa. Hence, the differences may be ignored when very accurate results are not critical.
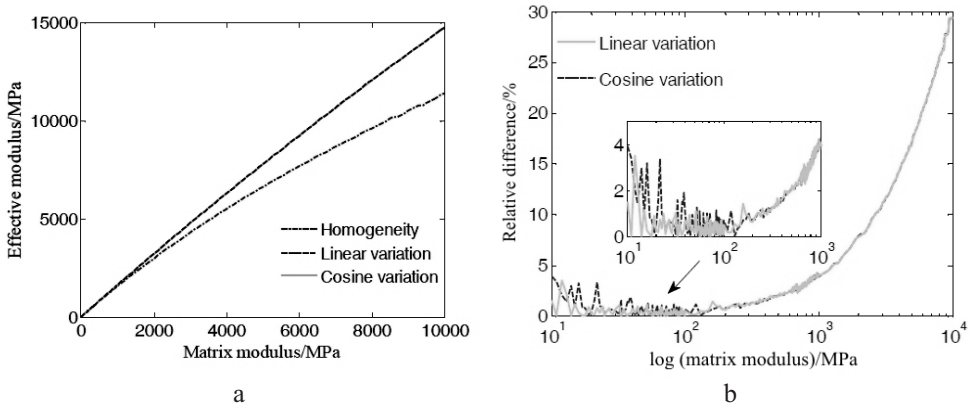
Fig. 9. Effect of matrix modulus on the effective modulus of CSP: (a) effective modulus; (b) semi-logarithmic plot.

Conclusions. To avoid the problem of dewetting, a proper bonding agent is added into CSP to improve the bonding strength between the matrix and inclusion. An ITZ will form around the inclusion particle. To understand the effects of ITZ on effective mechanical constants of CSP, the two-phase VCFEM is extended to three-phase VCFEM. The feasibility and effectiveness of this method are proved by comparing the displacement results of this method and the conventional finite element method. Based on the analysis of a 39 elements RVE model, we can find that with the increase of ITZ thickness, the modulus and Poisson's ratio of CSP are getting closer to that of inclusion. With the rise of inclusion volume fraction and matrix modulus, the effective modulus of homogeneous ITZ composites is getting smaller than that of inhomogeneous ITZ composites. However, relative differences between effective moduli of homogeneous and inhomogeneous ITZ composites are less than 4% when matrix modulus is not more than 100 MPa.

1. J. Xu, X. Chen, H. Wang, et al., "Thermo-damage-viscoelastic constitutive model of HTPB composite propellant," *Int. J. Solids Struct.*, **51**, No. 18, 3209–3217 (2014).

2. M. R. Taw and D. F. Bahr, "The mechanical properties of minimally processed RDX," *Propell. Explos. Pyrot.*, **42**, No. 6, 659–664 (2017).

3. P.-A. Toulemonde, J. Diani, P. Gilormini, et al., "Roles of the interphase stiffness and percolation on the behavior of solid propellants," *Propell. Explos. Pyrot.*, **41**, No. 6, 978–986 (2016).

4. J. P. Olivier, J. C. Maso, and B. Bourdette, "Interfacial transition zone in concrete," *Adv. Cem. Based Mater.*, **2**, No. 1, 30–38 (1995).

5. Z. Hanshin and P. J. M. Monteiro, "An inverse method to determine the elastic properties of the interphase between the aggregate and the cement paste," *Cement Concrete Res.*, **32**, No. 8, 1291–1300 (2002).

6. A. R. Brough and A. Atkinson, "Automated identification of the aggregate-paste interfacial transition zone in mortars of silica sand with Portland or alkali-activated slag cement paste," *Cement Concrete Res.*, **30**, No. 6, 849–854 (2000).

7. K. L. Scrivener, A. K. Crumbie, and P. Laugesen, "The interfacial transition zone (ITZ) between cement paste and aggregate in concrete," *Interface Sci.*, **12**, No. 4, 411–421 (2004).

8. F. Belaid, G. Arliguie, and R. François, "Porous structure of the ITZ around galvanized and ordinary steel reinforcements," *Cement Concrete Res.*, **31**, No. 11, 1561–1566 (2001).

9. J. D. Shane, T. Mason, H. Jennings, et al., "Effect of the interfacial transition zone on the conductivity of Portland cement mortars," *J. Am. Ceram. Soc.*, **83**, No. 5, 1137–1144 (2010).

10. C. Pei, Y. Yao, D. Chen, et al., "Experimental study of the tensile bond strength in concrete aggregate-paste interfacial transition zone," *Appl. Mech. Mater.*, **193–194**, No. 1384–1388 (2012).

11. J. J. Zheng, F. F. Xiong, Z. M. Wu, and W. L. Jin, "A numerical algorithm for the ITZ area fraction in concrete with elliptical aggregate particles," *Mag. Concrete Res.*, **61**, No. 2, 109–117 (2009).

12. Y. Gao, G. D. Schutter, G. Ye, and M. Zhang, "A preliminary numerical study on ITZ in cementitious composites," in: N. Kringos, B. Birgisson, D. Frost, and L. Wang (Eds.), *Multi-Scale Modeling and Characterization of Infrastructure Materials*, RILEM Bookseries, Vol. 8, Springer, Dordrecht (2013), pp. 99–108.

13. F. Bernard and S. Kamali-Bernard, "Numerical study of ITZ contribution on mechanical behavior and diffusivity of mortars," *Comp. Mater. Sci.*, **102**, 250–257 (2015).

14. S. Ghosh and S. N. Mukhopadhyay, "A two-dimensional automatic mesh generator for finite element analysis for random composites," *Comput. Struct.*, **41**, No. 2, 245–256 (1991).

15. S. Ghosh and S. N. Mukhopadhyay, "A material based finite element analysis of heterogeneous media involving Dirichlet tessellations," *Comput. Method. Appl. M.*, **104**, No. 2, 211–247 (1993).

16. S. Ghosh, K. Lee, and S. Moorthy, "Multiple scale analysis of heterogeneous elastic structures using homogenization theory and Voronoi cell finite element method," *Int. J. Solids Struct.*, **32**, No. 1, 27–62 (1995).

17. S. Ghosh and Y. Liu, "Voronoi cell finite element model based on micropolar theory of thermoelasticity for heterogeneous materials," *Int. J. Numer. Meth. Eng.*, **38**, No. 8, 1361–1398 (1995).

18. S. Ghosh and S. Moorthy, "Elastic-plastic analysis of arbitrary heterogeneous materials with the Voronoi Cell finite element method," *Comput. Method. Appl. M..*, **121**, Nos. 1-4, 373–409 (1995).

19. S. Ghosh, K. Lee, and P. Raghavan, "A multi-level computational model for multiscale damage analysis in composite and porous materials," *Int. J. Solids Struct.*, **38**, No. 14, 2335–2385 (2001).

20. P. M. Eder, J. E. Giuliani, and S. Ghosh, "Multilevel parallel programming for 3D Voronoi cell finite element modeling of heterogeneous materials," *Int. J. High Perform. C.*, **19**, No. 1, 29–45 (2005).

21. L. L. Shen, Z. B. Shen, H. Y. Li, and Z. Y. Zhang, "A Voronoi cell finite element method for estimating effective mechanical properties of composite solid propellants," *J. Mech. Sci. Technol.*, **31**, No. 11, 5377–5385 (2017).

22. W. Wang and I. Jasiuk, "Effective elastic constants of particulate composites with inhomogeneous interphases," *J. Compos. Mater.*, **32**, No. 15, 1391–1422 (1998).

23. S. J. Zhi, B. Sun, and J. W. Zhang, "Multiscale modeling of heterogeneous propellants from particle packing to grain failure using a surface-based cohesive approach," *Acta Mech. Sinica*, **28**, No. 3, 746–759 (2012).